Ultra-porous titanium nitride as a dual-action supercapacitor for implantable neural interfacing electrodes

Jeanelle Arpa [a], Kristian Rechendorff [b], Pierre Schembri Wismayer [c], Bertram Mallia [a,*]

[a] *Department of Metallurgy and Materials Engineering, Faculty of Engineering, University of Malta, Msida, Malta*
[b] *Danish Technological Institute, Århus, Denmark*
[c] *Department of Anatomy, Faculty of Medicine and Surgery, University of Malta, Msida, Malta*

HIGHLIGHTS

- Ultra-porous neural electrode based on over-stoichiometric titanium nitride.
- Electrode with combined electrochemical double layer- and pseudo-capacitance.
- Results show low impedance and high charge capacity.
- Sustained electrochemical performance for chronic applications.

GRAPHICAL ABSTRACT
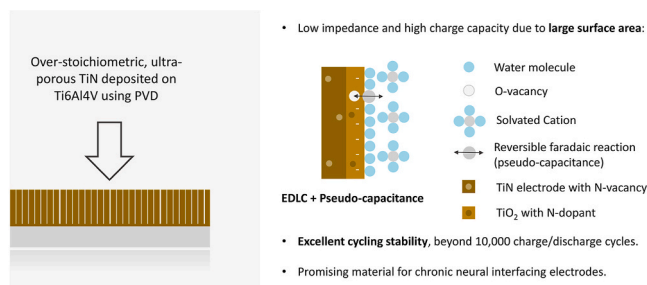
ABSTRACT

Frontier applications in implantable neural interfacing have raised the demand for low-impedance, high-charge-capacity electrodes capable of retaining these properties with chronic use. Herein, we evaluate an ultra-porous electrode based on over-stoichiometric titanium nitride for its application as a dual-action supercapacitor. Electrochemical measurements demonstrate both faradaic and non-faradaic capacitive mechanisms operating simultaneously, resulting in very high charge capacity with minimal impedance limitations. These characteristics were maintained over 10,000 charge-discharge cycles without significant loss in performance. Moreover, N-vacancies hypothesized to permit the reversible faradaic reactions on the electrode surface appear to remain stable, indicating that the film is able to renew its supply with each cycle, possibly by outward diffusion of excess N from the bulk and into the surface.

1. Introduction

The treatment, management and prognosis of various diseases, conditions, and injuries of the nervous system have benefited greatly in recent decades from advancements made in the field of implantable neural interfacing electrodes [1]. The ideal device is expected to be biocompatible, interface closely with the targeted tissue, withstand chemical and physical degradation, and exhibit ease of manufacture and implantation [2,3]. In the context of electrochemical performance, the two most important criteria that must be met are high charge capacity

---

and low electrical impedance, both of which should be maintained throughout the implant's lifetime [4,5]. As such, the materials employed for neural interfacing are generally discussed based on their charge transfer mechanism and their ability to retain it [6].

The first category of materials relies on the accumulation of electrical charge on their surfaces and ionic charge provided by solvated ions in solution. When the electrode is polarized, these charges form an inner and outer Helmholtz layer respectively, and molecules of solvent trapped between the layers act as a dielectric. In this way, the electrode functions as an electrostatic double-layer capacitor (EDLC) [2]. This being a purely physical process, EDLCs benefit from long-term cycling stability, making them the optimal choice in applications where sustained operation is the primary concern [7]. The associated disadvantage is spatial limitation, whereby the maximum attainable capacitance is capped by the size of the electrode/electrolyte interface. As a result, most research efforts aimed towards improving EDLCs are focused on maximizing effective surface area, usually through the introduction of porosity [8,9]. Much progress has been made in this regard, with developments such as titanium nitride nanopores [10], amorphous carbon nanotubes [11], and titania nanotube arrays [12] significantly improving electrode performance over conventional bulk electrodes. In these cases, the necessary balance between structural integrity and material porosity is an obvious drawback, and effectively limits the extent to which morphological changes can be employed before collapse [12,13].

The second category of materials, often termed pseudo-capacitors, permit electrochemical charge transfer across the electrode surface or near-surface. These faradaic reactions occur through rapid chemisorption or intercalation of charge-compensation ions in solution [14]. Some of the more prominent materials within this category are platinum [15], platinum-iridium alloys [16], and iridium oxide [17], all of which have been thoroughly researched and implemented in the past few decades. Contrary to EDLCs, the mechanisms of charge transfer are not solely dependent on physical phenomena, and thus their characteristics may be improved through alternative means [14]. Alloying, heat treatments, defect and stoichiometric control have all been employed towards this end with reasonable success [15,17,18]. Furthermore, as faradaic reactions on the electrode necessarily increase with access to surface area, pseudo-capacitors also benefit from the same strategies applied to EDLCs [10,14,19,20]. Owing to this, pseudo-capacitors typically outperform EDLCs in terms of initial charge capacity and low impedance, although they may be prone to significant deterioration with repeated cycling unless optimized [21].

The ongoing development of increasingly targeted therapies, often intended to function throughout the patient's lifetime, has intensified the demand for miniaturized electrodes with sustained capacitive function [1]. Accordingly, a device combining the assets of EDLCs and pseudo-capacitors is highly desirable in this regard. Emerging hybrid supercapacitors, high-capacity materials capable of both faradaic and non-faradaic charging, have made these goals more attainable in recent years [22]. Having widely demonstrated success in the energy storage and conversion sector, this material group shows great potential for neural interfacing [23]. Transition metal nitrides are a class of materials well-suited to this application, owing to their varied bonding (a combination of metallic, covalent, and ionic bonding) and special crystal structures comprising interstitial nitrogen atoms residing in a metal lattice. The resulting characteristics include varied valence states, extensive redox chemistry, and exceptionally low electrical impedances [23,24].

One candidate that combines these traits with good biocompatibility is over-stoichiometric titanium nitride, i.e., TiN_x where $x > 1$ [25,26]. A well-established EDLC, TiN has a reliable history as a neural interfacing electrode [27], with varied applications ranging from incontinence management [28] to motor control [29]. Improvements to its electrochemical properties have been achieved through morphological changes, from the development of thin films [30], to bulk material [31],

and open porous structures [32]. Unlike stoichiometric TiN, many research groups posit that TiN_x can additionally engage in reversible faradaic reactions, despite the lack of characteristic redox peaks in its cyclic voltammograms [17,18,32,33]. The origin of its faradaic charge transfer is generally attributed to the outward diffusion of loosely-bound N-atoms at the grain boundaries, whereby rapid oxidation occurs to produce N-doped TiO_2. This leads to the formation of O-vacancies in the oxide, likely through the act of charge compensation, which then engage in pseudo-capacitive reactions [34–37]. In combination with established double-layer capacitance, this mechanism drastically improves the performance of over-stoichiometric TiN and the material may thus be described as a dual-action supercapacitor [21]. Moreover, owing to the ease with which morphology and stoichiometry may be controlled during physical vapour deposition (PVD), chamber parameters may be wholly exploited to develop a TiN electrode that embodies both faradaic and non-faradaic charging whilst maximizing effective surface area. Primarily, the use of high N_2 partial pressures during deposition have been shown to result in highly-porous, over-stoichiometric films rich in excess N [38–40].

Herein we present a low-impedance and high-charge capacity neural electrode based on ultra-porous titanium nitride (TiN) films grown via PVD. High N_2 partial pressure is used to produce over-stoichiometric films with an open columnar structure that permits full electrolyte penetration for minimal diffusion-related limitations. The hybrid charging mechanisms are clearly demonstrated via exclusionary experiments, and are additionally shown to be highly reliable, exhibiting no significant degradation over 10,000 voltammetry cycles. These results establish the ultra-porous TiN as a viable candidate for neural interfacing, particularly in chronic applications requiring sustained electrical performance.

2. Materials and methods

2.1. Electrode fabrication

Grade 5 extra-low interstitial Ti6Al4V was chosen as the substrate material for the electrodes (Brindley Metals, UK). A layer of over-stoichiometric porous TiN was deposited via DC reactive magnetron sputtering using an industrial PVD coating unit (CC800/9 SiNOx, CemeCon AG, Germany). The coating was sputtered from four Ti targets (88×200 mm) of 99.5% purity in an Ar/N_2 atmosphere. The gas purity was 99.999% and the Ar/N_2 flow ratio was 400 sccm/350 sccm.

2.2. Characterization

Field emission scanning electron microscopy (FE-SEM) (Carl Zeiss: MerlinTM, Germany) was employed to analyse the surface and transverse morphology of the porous TiN films. Cross-sections were produced by cutting across the electrode with an Accutom-10 (Struers, Denmark) and preparing the exposed surface for analysis. Secondary electron images were taken using an acceleration voltage of 5 kV. ImageJ image processing and analysis software was used to estimate the surface porosity of the TiN film from the SEM images.

Bragg-Brentano X-ray diffraction data was collected using a Bruker D8 Advance X-Ray diffractometer (Bruker, Germany) equipped with a CuKα ($\lambda = 1.5406$ Å) radiation source. Measurements were taken at 21°C using a 40 kV acceleration voltage at a step size of 0.01° and dwell time of 2 s. Resultant peaks were fitted to corresponding phases using PDXL integrated X-ray powder diffraction software (Rigaku, Japan).

Micro-Raman spectroscopy of the TiN electrodes before and after electrochemical testing was carried out using a Raman microscope spectrometer (Horiba Scientific, Japan) operated at 21°C with 532 nm (green light) laser, 1800 grating, and 10 s acquisition time. 15 measurements were taken for each condition to ensure repeatability.

2.3. Electrochemistry

All electrochemical measurements were taken in protic and aprotic electrolytes; Dulbecco's phosphate buffered saline solution (PBS) (Oxoid, UK), and a 1 M organic solution of tetraethylammonium tetrafluoroborate (Et$_4$NBF$_4$) (Alfa Aesar, 99%), respectively. A conventional three-electrode cell was employed for testing, consisting of a 25 mm length of platinum wire (Advent, 99.95%) with 0.4 mm diameter as counter electrode, the TiN as working electrode, and a saturated KCl (Gamry, USA) or non-aqueous Ag/Ag+ (Ossila, UK) reference electrode in protic and aprotic solutions, respectively. A geometric surface area of 0.238 cm^2 on the TiN electrodes was exposed to the electrolytes for testing. Experiments were controlled using a computer driven Gamry Reference 600 potentiostat/galvanostat. All measurements were carried out at a physiological temperature of $37 \pm 2\,^{\circ}$C maintained by means of a heated water jacket.

Potentiostatic electrochemical impedance spectroscopy (EIS) was carried out at the open circuit potential with a sinusoidal voltage of amplitude 10 mV within the frequency range of 0.1 Hz–10 kHz. Equivalent circuit modelling and data fitting functions on the Gamry Echem Analyst software were employed to analyse resultant spectra. Cyclic voltammetry measurements were made by cycling the electrode voltage between the solvent electrolysis limits. These solvent window limits were determined by linear sweep voltammetry in the cathodic and anodic directions with respect to the OCP at a rate of 50 mV/s, until the emergence of a rapidly increasing current. Voltammograms were measured at sweep rates of 50, 100, 500 and 1000 mV/s, with 10 cycle measurements per sweep rate. The cathodic charge storage capacity (CSCc) was determined by integrating the area beneath the zero-current axis for the final cycle of each test. The sweep rates were chosen to assess the TiN electrodes under different experimental conditions, from the high charge/discharge rates associated with typical electrode operation (1000 mV/s), down to slower rates where the influence of pore resistance and ionic kinetic limitations are reduced (50 mV/s).

The coulombic efficiency (CE) of the electrodes at sweep rates of 1000 and 100 mV/s were calculated from the ratio of Q$_{discharge}$ and Q$_{charge}$, corresponding to the cathodic and anodic charge densities, respectively, as shown in Equation (1):

$$CE\ (\%) = \frac{Q_{discharge}}{Q_{charge}} \times 100 \qquad (1)$$

Lifetime analysis was carried out by subjecting the TiN films to 10,000 cyclic voltammetry cycles at 1000 mV/s while assessing changes in pseudo-capacitance. EIS measurements were taken intermittently at the beginning of the experiment and after each 1000 cycles. The tests were also conducted at a sweep rate of 100 mV/s. Although not representative of intended use, the latter experiments were carried out to observe electrode behaviour under conditions of high pseudo-capacitive demand. Both sets of analyses were conducted in PBS solution maintained at $37 \pm 2\,^{\circ}$C.

2.4. Statistics

All results are expressed as the mean $\pm$ standard deviation (SD). Regression analysis was used to determine whether trends exist in changes to capacitance during electrochemical cycling. The intensity ratios of Raman peaks with and without cycling were compared using t-tests. All statistical analysis was carried out using SPSS software, version 20.0 (SPSS, Inc., Chicago, IL, USA). A statistically significant difference was considered if $p < 0.05$.

3. Results and discussion

In this work, the morphology, crystal structure, and chemical state of the prepared TiN films were examined using SEM, XRD, and micro-Raman spectroscopy. SEM images of the electrode topography and cross-section are shown in Fig. 1. Film thickness measurements taken across 5 different electrode samples were found to be 9.5 ± 0.8 μm. The micrographs reveal a rough and porous topography with distinct pyramidal-shaped structures crowning disaggregated columns growing normal to the substrate and measuring ~500 nm across at their thickest point. The resultant electrodes had an average mass loading of 4.98 mg/cm^2.

The X-ray diffraction pattern for as-deposited TiN was measured between 2θ angles of 20–80° and is given in Fig. 2. The (111) and (222) peak positions were indexed to the cubic TiN phase (PDF no. 04-015-0336) having an FCC-like crystal structure with space group Fm-3m (225). The patterns reveal a highly textured coating with a preferred orientation along the (111) and corresponding (222) planes, situated at the 2θ values of 36.46° and 77.74°, respectively. Being the plane of lowest strain energy, prevalence of the (111) orientation is expected in thick TiN films (>150 nm), where strain energy dominates over surface energy. The crystallographic texture thus develops as a means to lower the total energy of the system [41]. This texturing effect is highly advantageous in the application of neural interfacing, as many research groups report increased surface roughness, and hence effective surface area, with increasing (111) orientation dominance [39,42,41].

The micro-Raman spectrum in the range of 50–700 cm^{-1} was collected for the electrodes using 532 nm green light laser and is shown in Fig. 3. In the case of TiN films, it has been previously shown that scattering in the acoustic range (~150-350 cm^{-1}) may be attributed to vibrations of the heavy Ti cations while that in the optical range (~550-650 cm^{-1}) is associated with vibrations of the lighter N anions [43]. With reference to the findings of other research groups, the peaks occurring at 152, 260, and 601 cm^{-1} may be respectively corresponded to the first-order transverse acoustic (TA), longitudinal acoustic (LA) and transverse optical (TO) vibrations of TiN [18,33,34,38]. In perfect crystal structures such as stoichiometric TiN, the detection of first order scattering is understood to be forbidden, as every ion in the crystal occupies a site of inversion symmetry. However, defects introduced into the crystal structure effectively disrupt this symmetry, causing atomic displacement in neighbouring atoms. As a result, their derivatives are non-zero and thus first-order polarizable [44]. In addition to randomly occurring imperfections in the crystal, deviations from stoichiometry impart numerous defects within the TiN structure, thereby allowing first-order detection. In this case, each peak is a representation of the defect that induced it, i.e., acoustic and optical peaks indicate nitrogen and titanium vacancies in the lattice, respectively [43]. Thus, assessing the relative intensities of the transverse acoustic (TA) and optical (TO) peaks may provide an indication of the defect ratio in the film [19]. Since acoustic scattering dominates over optical transmissions, and thus I$_{TO}$/I$_{TA}$<1, it may be concluded that N-vacancies comprise the majority of defects in the bulk of the electrode.

Although at the outset it appears contradictory that N-vacancies prevail in N-rich TiN, some factors may be considered to corroborate this result. Primarily, it is understood that in over-stoichiometric TiN, the loosely bound N at grain boundaries permit rapid oxidation even at room temperature, as the reaction of TiN with O$_2$ is thermodynamically favourable [37,44]. Supporting this statement are three further peaks in the Raman spectrum ascribable to anatase TiO$_2$, which occur at 205, 410, and 519 cm^{-1}. These peaks, closely associated with β-N doped TiO$_2$ (hereafter denoted as N–TiO$_2$) as indicated by literature, can only be detected within a narrow spectrum of laser wavelengths [34,45]. The green light laser used in this study carries an energy of 2.33 eV, which is similar to the band gap of N–TiO$_2$ (2.2–2.6 eV) [46]. This results in a resonance effect, and thus the peaks of the oxide may be recorded [35]. Attempts to replicate these measurements using a 785 nm wavelength were in fact unsuccessful, as only peaks associated with TiN were detected as shown in Fig. 4. Congruently, if β-N dopants are present in the oxide, the prevalence of N-vacancies in the bulk is validated, as many research groups posit the outwards diffusion and incorporation of excess N-atoms into the growing oxide [17,34,35].
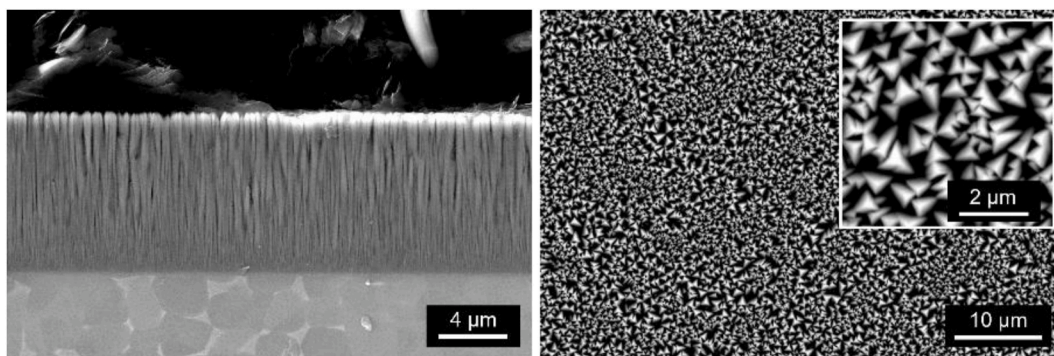
Fig. 1. Cross-sectional morphology (left) and surface topography (right) SEM images of the ultra-porous TiN deposited onto Ti6Al4V.
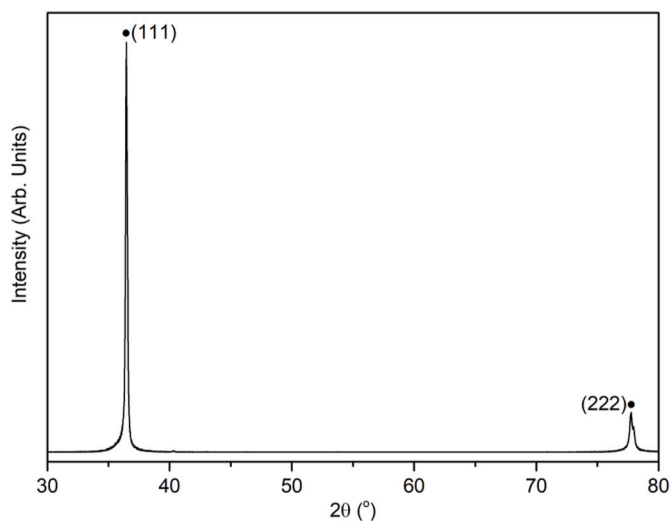

Fig. 2. Bragg Brentano XRD pattern for TiN electrode. Miller indices for cubic TiN are labelled (PDF no. 04-015-0336).
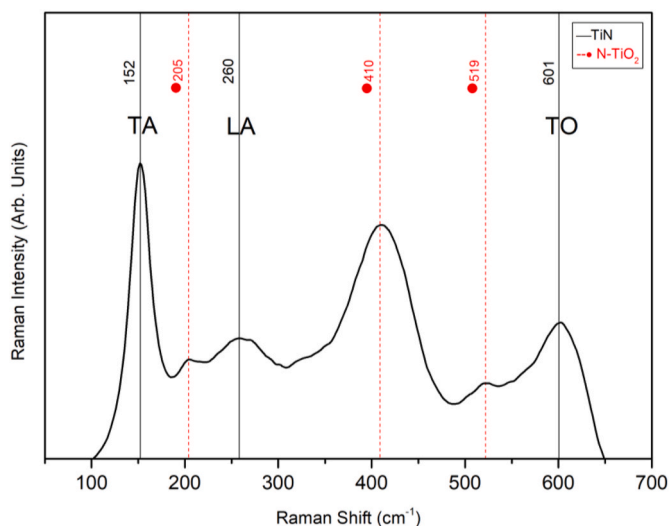

Fig. 3. Raman spectrum collected for untested TiN electrode using 532 nm laser wavelength. Identified peaks were corresponded to acoustic and optical modes of TiN (black), as well as N-doped Anatase TiO_2 (red). (For interpretation of the references to colour in this figure legend, the reader is referred to the Web version of this article.)
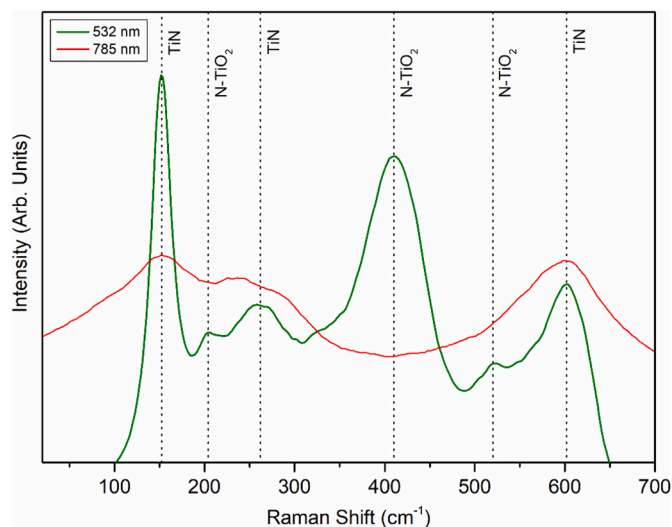

Fig. 4. Raman spectra of untested TiN electrodes. Measurements were taken using laser wavelengths of 532 nm (green) and 785 nm (red). Peaks typically associated with $N–TiO_2$ appear when using a laser wavelength of 532 nm but are notably absent when using a wavelength of 785 nm. (For interpretation of the references to colour in this figure legend, the reader is referred to the Web version of this article.)

Ultimately, the development of $N–TiO_2$ is a desired characteristic when considering TiN for chronic neural interfacing; N-doping triggers the induction of O-vacancies through the effect of charge compensation. In turn, these vacancies can engage in reversible faradaic reactions that, in combination with traditional double layer capacitance, greatly boost capacitive ability [34–37]. Thus, the suspected O-vacancies, coupled with the evident porous architecture of the TiN film, was expected to exhibit excellent electrochemical properties.

To demonstrate this phenomenon, EIS and CV measurements were taken in two different electrolytes to permit distinction between pseudo-capacitance and double-layer capacitance. Previous studies have reliably shown that pseudo-capacitance is affected only by the protons and cations in solution, and thus the electrolytes employed in this work were chosen accordingly [33,46]. To simulate the physiological condition, under which both mechanisms are assumed to operate, tests were conducted in aqueous PBS solution. Conversely, a non-protonated organic solution of 1 M Et_4NBF_4 in acetonitrile was used to inhibit reversible faradaic reactions. Coupled with the lack of protons, the bulky Et_4N^+ cation is spatially limited, and thus restricted from participating in pseudo-capacitance.

Bode and Nyquist spectra recorded during EIS measurements are plotted in Fig. 5. A basic Randles Circuit consisting of double layer capacitance, CPE_{dl} in parallel with resistance to faradaic charge transfer,
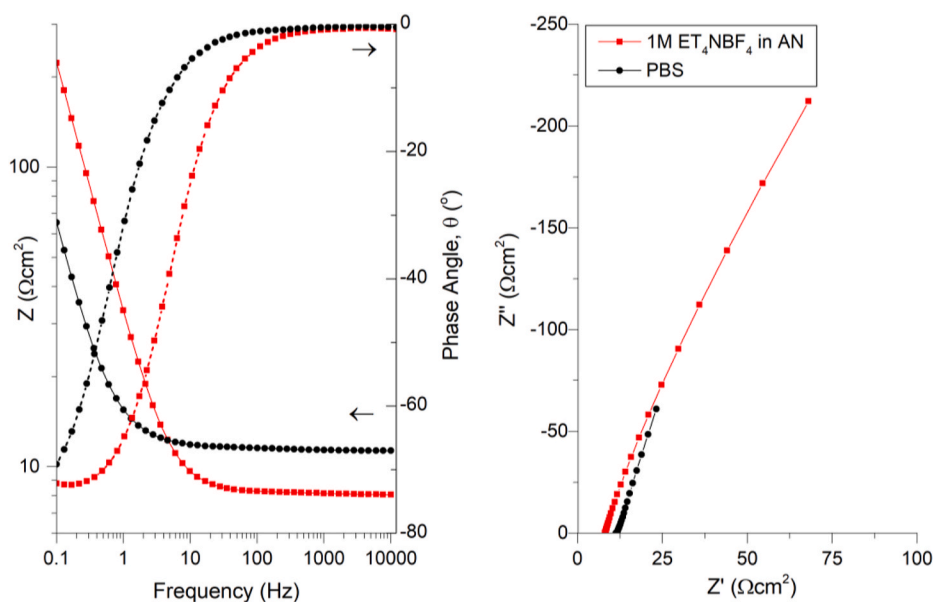
Fig. 5. Resultant EIS spectra, showing Bode (left) and Nyquist (right) plots for TiN electrodes tested in PBS (black) and 1 M Et₄NBF₄ solution in acetonitrile.

R_F, both in series with solution resistance, R_s, was sufficient to model the spectra obtained in organic electrolyte. An identical circuit could not adequately model spectra obtained in PBS solution, predominantly due to incongruency in the low frequency domain. In such cases a Warburg impedance is commonly included in the equivalent circuits of porous materials to account for diffusion limitations within the narrow, inaccessible channels. However, the characteristic $45°$ angle associated with this phenomenon is not evident in the resulting spectra, indicating good ionic mobility within the pores of the TiN film. Instead, the approximate angle of $75°$ suggests the imperfect capacitive behaviour typically associated with pseudo-capacitance. A constant phase element CPE_{pseu} (Y_{pseu}, α_{pseu}) was thus placed in series with R_F, where Y_{pseu} acts as a stand-in for pseudo-capacitance, and α_{pseu} is an empirical constant representing deviation from ideal behaviour (ie, when $\alpha = 1$), usually due to leakage current. In both models, the double layer capacitors are also replaced with constant phase elements, having variables Y_{dl} and α_{dl}. In this case the Y_{dl} is a stand-in for double layer capacitance, and α_{dl} represents deviation from ideal behaviour, potentially due to non-ideal layer formation, leakage current, or influence from surface roughness. Both circuits are given in Fig. 6.

Values extracted from fitting the equivalent circuit models are given in Table 1. The different behaviour of the TiN films in the two electrolytes is readily apparent, with a three-fold increase in impedance at 0.1 Hz for measurements taken in Acetonitrile. The Y_{dl} in PBS was found to be slightly lower than that measured in organic solution, and as such the double layer capacitance was ruled out as an influencing factor on the

Table 1
EIS results from curve fitting of equivalent circuit models for tests conducted in PBS and 1 M Et₄NBF₄ solution in Acetonitrile. The average of five readings is given with standard deviation from the mean.

Test Solution		
Element	PBS	1 M Et₄NBF₄ in AN
R_s, Ωcm^2	14.9 ± 3.1	7.6 ± 0.4
Y_{dl}, mSs^acm²	3.9 ± 0.7	7.1 ± 2.7
α_{dl}	0.855 ± 0.024	0.868 ± 0.019
Y_{pseu}, mSs^acm²	14.7 ± 3	/
α_{pseu}	0.879 ± 0.007	/
R_f, $\Omega cm2$	1.5 ± 0.5	2537.9 ± 840
$|Z|$ at 0.1Hz, Ωcm^2	79.5 ± 14.4	248.3 ± 57.5

increased impedance in acetonitrile. As pseudo-capacitance is the phenomenon through which faradaic charge transfer is enabled, an environment which inhibits its action would necessarily result in a larger R_F. This was the case for tests conducted in acetonitrile where R_F was calculated at 2537 Ωcm^2, a large figure when compared to the 1.5 Ωcm^2 measured in PBS. This highlights the dominant role of pseudo-capacitance in lowering the electrode's overall impedance at low frequencies. Furthermore, it strongly corroborates the observations made via Raman analysis, lending credence to the theorized role of overstoichiometry in permitting reversible faradaic reactions.

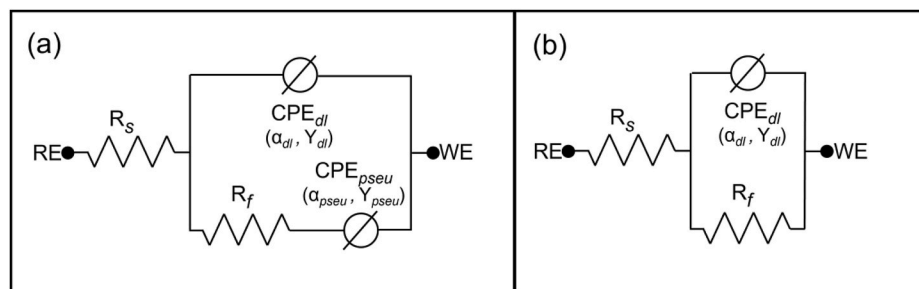The impact of pseudo-capacitance on electrochemical performance

Fig. 6. Circuits used to model resulting EIS spectra after testing TiN electrodes in PBS (a) and 1 M Et₄NBF₄ solution in acetonitrile (b), where the following parameters are used: reference electrode (RE), working electrode (WE), solution resistance (R_s), resistance to faradaic charge transfer (R_F), double layer capacitance (CPE_{dl}, a constant phase element further described by α_{dl} and Y_{dl}), and pseudo-capacitance (CPE_{pseu}, a constant phase element further described by α_{pseu} and Y_{pseu}).

was further studied by performing CV tests in the same two solutions. Representative voltammograms measured at sweep rates of 50, 100, 500, and 1000 mV/s in both electrolytes are given in Fig. 7, and the average calculated CSC_C are presented in Table 2. The cathodic and anodic working limits were found to be −0.6 and 0.9 V *vs* SCE respectively, and all voltammograms are presented between these values. With respect to measurements made in PBS solution, the voltammograms at low scan rates (≤500 mV/s) display the typical rectangular shape associated with a quasi-ideal capacitor. The shape is lost at faster sweep rates, adopting the slanted, diagonal representation of an ohmic-type conductor. Previous studies on highly-porous TiN have wholly attributed this phenomenon to the large ohmic drop that forms across pores, rendering the deeper sections of the channels redundant [39,47]. Analysing the results for organic electrolyte affirms the influence of porosity, as CSC_C values drop by ~45% as the scan rate is increased from 50 to 1000 mV/s. However, it is notable that the drop in acetonitrile is not equivalent to that in PBS, which was calculated at ~58%. Considering the observations made from EIS results, where it was shown that changing electrolyte has no significant impact on the electrochemical characteristics of the double layer, this discrepancy may be attributed to a larger influence on the pseudo-capacitance. Specifically, it highlights the kinetic limitations associated with reversible faradaic reactions as compared to the double layer. Despite this, the ultra-porous TiN still

Table 2

Cathodic charge storage capacity (CSC_C) for tests in PBS and in a 1 M solution of Et_4NBF_4 in Acetonitrile, measured at scan rates of 50, 100, 500 and 1000 mV/s. The average of five readings is given with standard deviation from the mean. The approximate % difference in charge storage between tests conducted at 50 and 1000 mV/s for the same electrolyte are also given.

CSC_C (mC/cm^2)		
Scan Rate (mV/s)	PBS	1 M Et_4NBF_4 in AN
50	53 ± 6	11 ± 3
100	46 ± 5	9 ± 2
500	30 ± 3	7 ± 1
1000	22 ± 3	6 ± 1
% Drop from 50 to 1000 mV/s	**58**	**45**

outperforms many of the electrode materials currently in use for neural interfacing in the form of higher charge capacity and lower impedance, including platinum/iridium (Pt/Ir) alloys [16] and iridium oxide (IrOx) [17], as well as some frontier materials like porous graphene [48] and poly(3,4-ethylenedioxythiophene)-poly(styrenesulfonate) (PEDOT:PSS) [49]. These findings emphasize the advantages of designing hybrid-capacitance electrodes over pure EDLC's or pseudo-capacitors.

When assessing applicability for chronic interfacing, the retention of capacitive mechanisms over numerous cycles is necessary. With a high
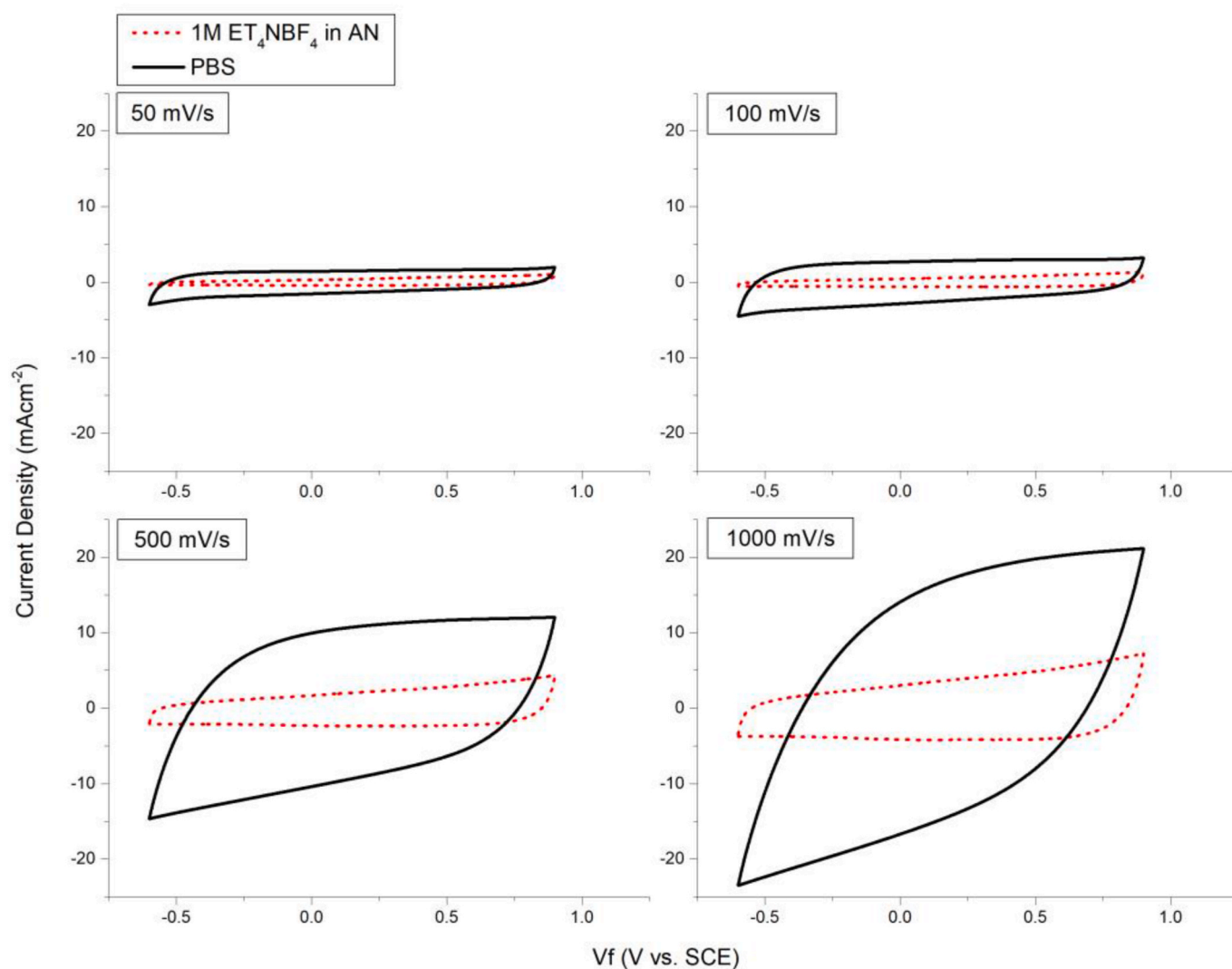
Fig. 7. Cyclic voltammograms of TiN electrodes tested at different sweep rates (50, 100, 500, and 100 mV/s) in PBS (black, solid) and 1 M Et_4NBF_4 solution in acetonitrile (red, dotted). (For interpretation of the references to colour in this figure legend, the reader is referred to the Web version of this article.)

coulombic efficiency (CE) of $99.68 \pm 0.06\%$ (calculated using Equation (1)) at a sweep rate of 1000 mV/s, the electrodes were expected to demonstrate a high level of reversibility during the charge/discharge process. To assess this, the TiN was subjected to 10,000 CV cycles at 1000 mV/s within the previously defined water window limits (-0.6 to 0.9 V *vs* SCE). PBS solution was chosen to permit monitoring of CPE_{pseu} and CPE_{dl} in tandem. EIS measurements were taken every 1000 cycles to quantify any resulting changes. Using the equivalent circuit model given in Fig. 6a to analyse the EIS spectra, CPE values (Y and α) were derived and plotted as a function of cycle number, as shown in Fig. 8 and Fig. 9. Regression analysis showed no significant drop ($p > 0.05$) in either Y_{pseu} or Y_{dl} over 10,000 consecutive cycles, nor any change in α_{pseu} and α_{dl}. Moreover, the electrode displayed very high charge retention, as shown in Fig. 10, with no statistically significant decrease ($p > 0.05$) being recorded. While such a high level of cycling stability is common for EDLC's, it is relatively exceptional in pseudo-capacitors [21]. Performing micro-Raman analysis on the electrodes additionally shows no appreciable change in chemical makeup after 10,000 cycles. In fact, quantifying and comparing the relative intensities I_{TO}/I_{TA} before and after cycling, as presented in Fig. 11, shows no statistically significant change ($p > 0.05$).

These results would imply that the number of oxygen vacancies in the $N-TiO_2$ remains stable despite repeated oxidation during cycling and, by extension, that the relative number of N-vacancies in the TiN sub-surface is also maintained. In this regard, Achour et al. [35] have proposed that the bulk TiN acts as a reservoir for β-N dopants, diffusing out into the oxide and creating new O-vacancies to replace the ones oxidized by electrochemical cycling. Concomitantly, atomic oxygen generated through this process diffuses downwards into the bulk TiN, healing N-vacancies while the oxide grows. In this way, the relative number of nitrogen and oxygen vacancies is stable, and pseudo-capacitance is maintained. To assess the applicability of this theory in explaining the observed results, the experiment was modified to intentionally exhaust the material's pseudo-capacitive mechanism. A cycling rate of 100 mV/s, at which the coulombic efficiency drops to $99.06 \pm 0.52\%$, was chosen to maximize engagement of redox-active sites (O-vacancy sites) on the electrode whilst keeping the test durations reasonably short (<5 days). All other parameters were maintained as per the previous experiment.
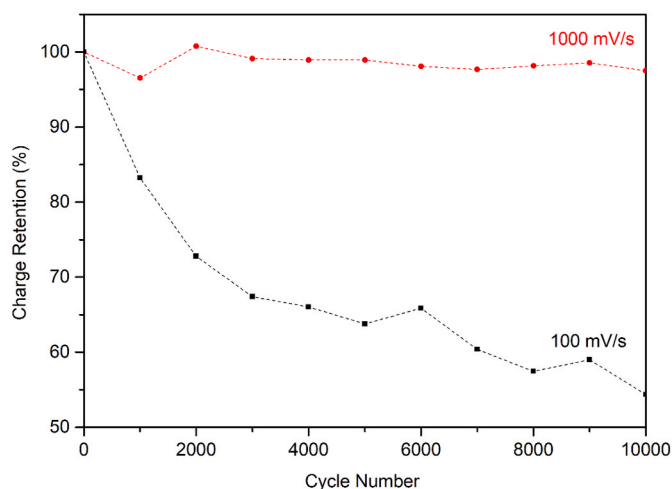
As shown in Fig. 8, a clear negative correlation ($p < 0.05$) between cycle number and Y_{pseu} exists, with an average drop of 46% recorded over 10,000 cycles. As with the 1000 mV/s tests, no significant change
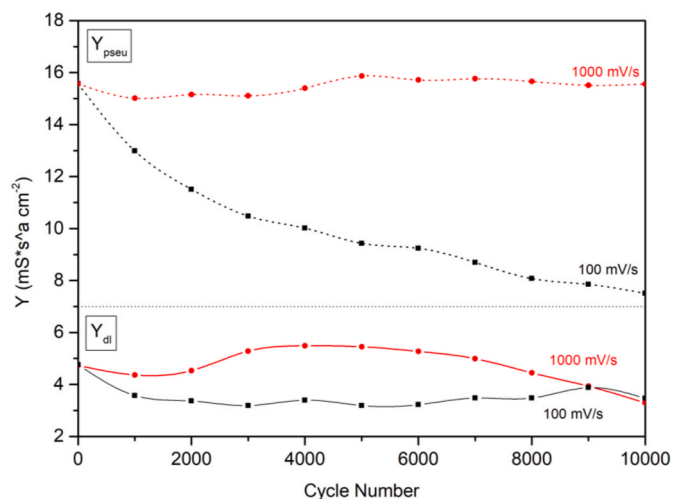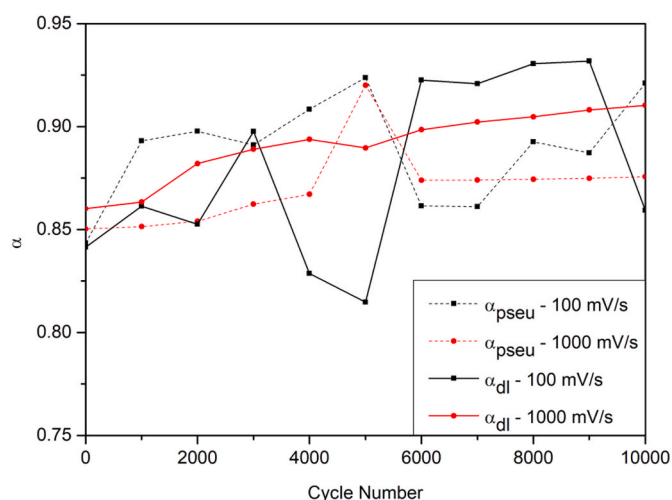
Fig. 9. Changes in α_{pseu} (dashed line) and α_{dl} (solid line) with number of cyclic voltammetry cycles carried out at 100 mV/s (black) and 1000 mV/s (red) in PBS. (For interpretation of the references to colour in this figure legend, the reader is referred to the Web version of this article.)

Fig. 10. Change in percentage (%) charge retention with number of cyclic voltammetry cycles carried out at 100 mV/s (black) and 1000 mV/s (red) in PBS. (For interpretation of the references to colour in this figure legend, the reader is referred to the Web version of this article.)
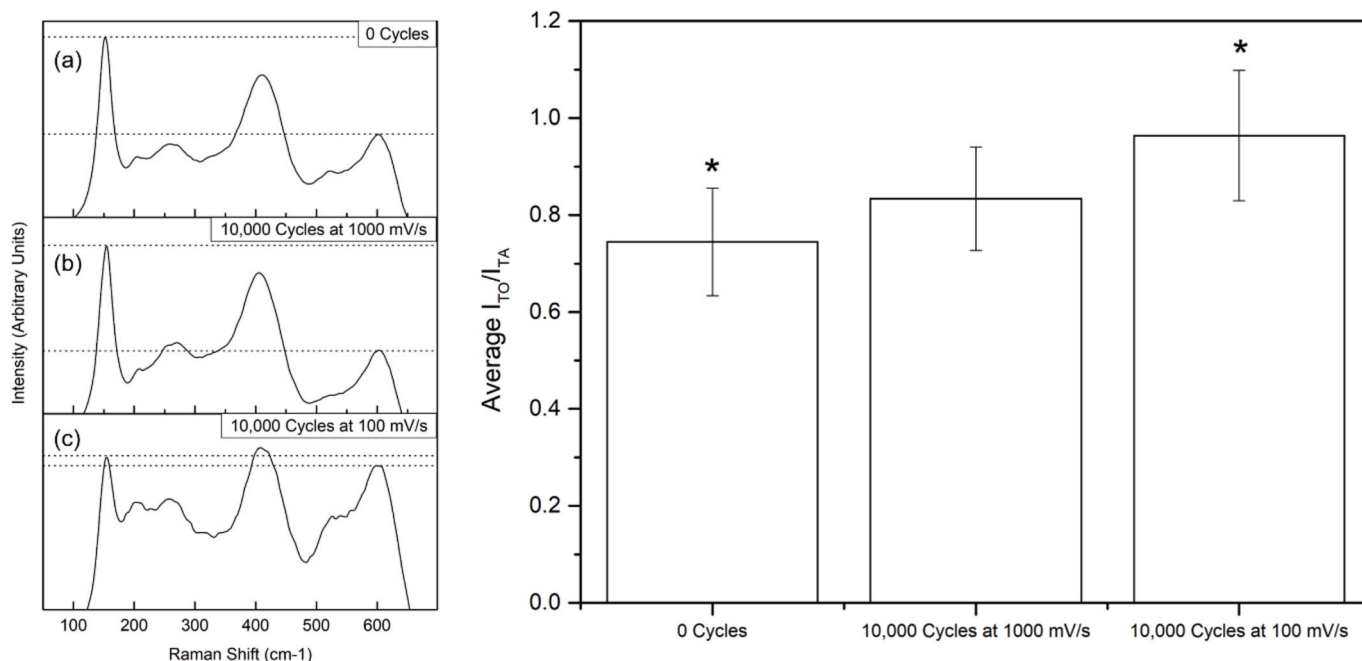
($p > 0.05$) was observed for Y_{dl} with cycling, and behavior does not differ meaningfully between the two conditions. The α_{pseu} and α_{dl}, shown in Fig. 9, also exhibit no significant change ($p > 0.05$), suggesting that the decline in electrode performance is unlikely to be related to increased current 'leakage'. Conversely, charge retention drops down to 54% by the 10,000th cycle (Fig. 10), clearly demonstrating the incomplete reversibility of the pseudo-capacitive process at low scan rates. The micro-Raman spectra for the electrodes were collected after the tests, and the I_{TO}/I_{TA} ratio calculated and compared to that of untested TiN. A significant change ($p < 0.05$) in the relative intensity of the 152 cm^{-1} peak is evident, dropping by an average of 22.7% after cycling.

The marked decrease in N-vacancies may therefore be reliably linked to the change in pseudo-capacitance, and a strong case can be made for the hypothesis outlined above. By extension, it can be inferred that the excellent performance of the TiN electrode is reliant on its over-stoichiometry, whereby pseudo-capacitive mechanisms are enabled through a balanced ratio of nitrogen and oxygen vacancies in the TiN bulk and TiO_2 oxide, respectively. Moreover, these properties are retained over numerous charge/discharge cycles when executed under

Fig. 8. Changes in Y_{pseu} (top) and Y_{dl} (bottom) with number of cyclic voltammetry cycles carried out at 100 mV/s (black) and 1000 mV/s (red) in PBS. (For interpretation of the references to colour in this figure legend, the reader is referred to the Web version of this article.)

Fig. 11. Image on the left shows the Raman spectra for TiN electrodes collected after 0 (a) and 10,000 cyclic voltammetry cycles at a sweep rate of either 1000 (b) or 100 mV/s (c). Chart on the right shows the average I_{TO}/I_{TA} ratios calculated from 25 readings for each condition. Error bars represent the standard deviation from the mean. * Indicates a statistically significant difference ($p < 0.05$).

conditions similar to those employed *in vivo*. These reversible faradaic reactions act in tandem with double layer capacitance, itself expanded through the film's porous architecture, to permit the large charge storage capacities and very low impedances that are crucial in neural interfacing.

4. Conclusions

In this work we develop a low-impedance, high-charge-capacity neural interfacing electrode based on ultra-porous, over-stoichiometric TiN film grown via PVD. Characterization revealed an open, columnar microstructure with an abundance of N-vacancies detected in the material sub-surface, thus indicating the potential for pseudo-capacitive behavior. The TiN demonstrated excellent electrochemical behavior in physiological electrolyte, with impedance and capacitance measurements equaling and, in some cases, even surpassing those of lead competing materials. Similar tests carried out in non-protonated electrolyte clearly demonstrate the large role pseudo-capacitance plays towards electrode performance, by suppressing its action and observing the corresponding changes in impedance and charge measurements. Aggressive cycling in protonated electrolyte resulted in lower detectable N-vacancies that were corresponded to drops in charge capacity and increased impedance, thus strengthening the theorized relationship between over-stoichiometry, vacancies, and reversible faradaic reactions on the TiN surface. Moreover, the electrode was also subjected to 10,000 cycles in physiological media at rates similar to those of operation *in vivo*, resulting in no significant physical, chemical, or electrochemical deterioration. Thus, in combination with the double layer, the large recorded pseudo-capacitance and its retention with cycling highlight the ultra-porous TiN as an excellent dual-action supercapacitor for use in neural interfacing. Further work employing test conditions that mimic more closely the clinical application, including the use of a two-electrode setup and the addition of proteins in the electrolyte, should be considered to study their influence on the electrode performance.

CRediT authorship contribution statement

Jeanelle Arpa: Conceptualization, Methodology, Validation, Formal analysis, Investigation, Data curation, Writing – original draft, Visualization, Funding acquisition. **Kristian Rechendorff:** Conceptualization, Resources, Writing – review & editing. **Pierre Schembri Wismayer:** Conceptualization, Writing – review & editing, Supervision, All authors have read and agreed to the published version of the manuscript. **Bertram Mallia:** Conceptualization, Validation, Resources, Writing – review & editing, Supervision, Project administration.

Declaration of competing interest

The authors declare that they have no known competing financial interests or personal relationships that could have appeared to influence the work reported in this paper.

Acknowledgements

References

[1] C. Russell, A.D. Roche, S. Chakrabarty, Peripheral nerve bionic interface: a review of electrodes, Int. J. Intell. Robot. Appl. 3 (1) (2019) 11–18, https://doi.org/10.1007/s41315-019-00086-3.

[2] N. Chen, et al., Neural interfaces engineered via micro- and nanostructured coatings, Nano Today 14 (2017) 59–83, https://doi.org/10.1016/j.nantod.2017.04.007.

[3] C. Günter, J. Delbeke, M. Ortiz-Catalan, Safety of long-term electrical peripheral nerve stimulation: review of the state of the art, J. NeuroEng. Rehabil. 16 (1) (2019) 1–16, https://doi.org/10.1186/s12984-018-0474-8.

[4] K.A. Sillay, et al., Long-term surface electrode impedance recordings associated with gliosis for a closed-loop neurostimulation device, Ann. Neurosci. 25 (4) (2019) 289–298, https://doi.org/10.1159/000481805.

[5] A. Campbell, C. Wu, Chronically implanted intracranial electrodes: tissue reaction and electrical changes, Micromachines 9 (9) (2018) 1–14, https://doi.org/10.3390/mi9090430.

[6] C. Keogh, Optimizing the neuron-electrode interface for chronic bioelectronic interfacing, Neurosurg. Focus 49 (1) (2020) 1–8, https://doi.org/10.3171/2020.4.FOCUS20178.

[7] V. Augustyn, P. Simon, B. Dunn, Pseudocapacitive oxide materials for high-rate electrochemical energy storage, Energy Environ. Sci. 7 (5) (2014) 1597–1614, https://doi.org/10.1039/c3ee44164d.

[8] H. Park, P. Takmakov, H. Lee, Electrochemical evaluations of fractal microelectrodes for energy efficient neurostimulation, Sci. Rep. 8 (1) (2018) 1–11, https://doi.org/10.1038/s41598-018-22545-w.

[9] N. Parveen, S.A. Ansari, M.Z. Ansari, M.O. Ansari, Manganese oxide as an effective electrode material for energy storage: a review, Environ. Chem. Lett. 20 (1) (2022) 283–309, https://doi.org/10.1007/s10311-021-01316-6.

[10] Y. Xie, Y. Wang, H. Du, Electrochemical capacitance performance of titanium nitride nanoarray, Mater. Sci. Eng. B Solid-State Mater. Adv. Technol. 178 (20) (2013) 1443–1451, https://doi.org/10.1016/j.mseb.2013.09.005.

[11] S. Jain, A. Sharma, B. Basu, Vertical electric field stimulated neural cell functionality on porous amorphous carbon electrodes, Biomaterials 34 (37) (2013) 9252–9263, https://doi.org/10.1016/j.biomaterials.2013.08.057.

[12] D. Khudhair, et al., Enhancement of electro-chemical properties of TiO2 nanotubes for biological interfacing, Mater. Sci. Eng. C 77 (2017) 111–120, https://doi.org/10.1016/j.msec.2017.03.112.

[13] W.A. Abbas, et al., Recent advances in the use of TiO2 nanotube powder in biological, environmental, and energy applications, Nanoscale Adv. 1 (8) (2019) 2801–2816, https://doi.org/10.1039/c9na00339h.

[14] J. Wang, et al., Pseudocapacitive materials for electrochemical capacitors: from rational synthesis to capacitance optimization, Natl. Sci. Rev. 4 (1) (2017) 71–90, https://doi.org/10.1093/nsr/nww072.

[15] C. Boehler, T. Stieglitz, M. Asplund, Nanostructured platinum grass enables superior impedance reduction for neural microelectrodes, Biomaterials 67 (2015) 346–353, https://doi.org/10.1016/j.biomaterials.2015.07.036.

[16] I.R. Cassar, et al., Electrodeposited platinum-iridium coating improves in vivo recording performance of chronically implanted microelectrode arrays, Biomaterials 205 (2019) 120–132, https://doi.org/10.1016/j.biomaterials.2019.03.017. Electrodeposited.

[17] Q. Zeng, K. Xia, B. Sun, Y. Yin, T. Wu, M.S. Humayun, Electrodeposited iridium oxide on platinum nanocones for improving neural stimulation microelectrodes, Electrochim. Acta 237 (2017) 152–159, https://doi.org/10.1016/j.electacta.2017.03.213.

[18] B.M. Gray, A.L. Hector, M. Jura, J.R. Owen, J. Whittam, Effect of oxidative surface treatments on charge storage at titanium nitride surfaces for supercapacitor applications, J. Mater. Chem. 5 (9) (2017) 4550–4559, https://doi.org/10.1039/C6TA08308K.

[19] A. Achour, et al., Role of nitrogen doping at the surface of titanium nitride thin films towards capacitive charge storage enhancement, J. Power Sources 359 (2017) 349–354, https://doi.org/10.1016/j.jpowsour.2017.05.074.

[20] S.A. Ansari, N. Parveen, M.A.S. Al-othoum, M.O. Ansari, Effect of washing on the electrochemical performance of a three-dimensional current collector for energy storage applications, Nanomaterials 11 (6) (2021), https://doi.org/10.3390/nano11061596.

[21] Y. Jiang, J. Liu, Definitions of pseudocapacitive materials: a brief review, Energy Environ. Mater. 2 (1) (2019) 30–37, https://doi.org/10.1002/eem2.12028.

[22] D.P. Chatterjee, A.K. Nandi, A review on the recent advances in hybrid supercapacitors, J. Mater. Chem. 9 (29) (2021) 15880–15918, https://doi.org/10.1039/d1ta02505h.

[23] M. Han, et al., Organic photovoltaic pseudocapacitors for neurostimulation, ACS Appl. Mater. Interfaces 12 (38) (2020) 42997–43008, https://doi.org/10.1021/acsami.0c11581.

[24] Y. Zhou, W. Guo, T. Li, A review on transition metal nitrides as electrode materials for supercapacitors, Ceram. Int. 45 (17) (2019) 21062–21076, https://doi.org/10.1016/j.ceramint.2019.07.151.

[25] J. Shi, et al., Review of transition metal nitrides and transition metal nitrides/carbon nanocomposites for supercapacitor electrodes, Mater. Chem. Phys. 245 (December 2019) (2020), 122533, https://doi.org/10.1016/j.matchemphys.2019.122533.

[26] C.C. Chien, K.T. Liu, J.G. Duh, K.W. Chang, K.H. Chung, Effect of nitride film coatings on cell compatibility, Dent. Mater. 24 (7) (2008) 986–993, https://doi.org/10.1016/j.dental.2007.11.020.

[27] S.F. Cogan, Neural stimulation and recording electrodes, Annu. Rev. Biomed. Eng. 10 (2008) 275–309, https://doi.org/10.1146/annurev.bioeng.10.061807.160518.

[28] S. Meijs, M. Fjorback, C. Jensen, S. Sørensen, K. Rechendorff, N.J.M. Rijkhoff, Influence of fibrous encapsulation on electro-chemical properties of TiN electrodes, Med. Eng. Phys. 38 (5) (2016) 468–476, https://doi.org/10.1016/j.medengphy.2016.02.010.

[29] E.K. Brunton, et al., In vivo comparison of the charge densities required to evoke motor responses using novel annular penetrating microelectrodes, Front. Neuroeng. 8 (2015) 1–11, https://doi.org/10.3389/fnins.2015.00265. MAY.

[30] M.A. González-González, et al., Thin film multi-electrode softening cuffs for selective neuromodulation, Sci. Rep. 8 (1) (2018) 1–15, https://doi.org/10.1038/s41598-018-34566-6.

[31] M. Canillas, B. Moreno, M. Carballo-Vila, J.R. Jurado, E. Chinarro, Bulk Ti nitride prepared from rutile TiO 2 for its application as stimulation electrode in neuroscience, Mater. Sci. Eng. C 96 (February 2018) (2019) 295–301, https://doi.org/10.1016/j.msec.2018.11.030.

[32] R. Sait, S. Govindarajan, R. Cross, Nitridation of optimised TiO2 nanorods through PECVD towards neural electrode application, Materialia 4 (September) (2018) 127–138, https://doi.org/10.1016/j.mtla.2018.09.015.

[33] D. Choi, P.N. Kumta, Nanocrystalline TiN derived by a two-step halide approach for electrochemical capacitors, J. Electrochem. Soc. 153 (12) (2006) A2298, https://doi.org/10.1149/1.2359692.

[34] G. Hasegawa, et al., Impact of electrolyte on pseudocapacitance and stability of porous titanium nitride (TiN) monolithic electrode, J. Electrochem. Soc. 162 (1) (2015), https://doi.org/10.1149/2.0491501jes. A77–A85.

[35] A. Achour, et al., Hierarchical nanocomposite electrodes based on titanium nitride and carbon nanotubes for micro-supercapacitors, Nano Energy 7 (2014) 104–113, https://doi.org/10.1016/j.nanoen.2014.04.008.

[36] E. Kao, C. Yang, R. Warren, A. Kozinda, L. Lin, ALD titanium nitride on vertically aligned carbon nanotube forests for electrochemical supercapacitors, Sensor Actuator Phys. 240 (2016) 160–166, https://doi.org/10.1016/j.sna.2016.01.044.

[37] C. Di Valentin, et al., N-doped TiO2: theory and experiment, Chem. Phys. 339 (1–3) (2007) 44–56, https://doi.org/10.1016/j.chemphys.2007.07.020.

[38] S. Logothetidis, A. Barborica, In-situ and real time room temperature oxidation studies of fcc TiN thin films, Microelectron. Eng. 33 (1–4) (1997) 309–316, https://doi.org/10.1016/s0167-9317(96)00059-7.

[39] N.K. Ponon, et al., Effect of deposition conditions and post deposition anneal on reactively sputtered titanium nitride thin films, Thin Solid Films 578 (2015) 31–37, https://doi.org/10.1016/j.tsf.2015.02.009.

[40] L.T. Cunha, P. Pedrosa, C.J. Tavares, E. Alves, F. Vaz, C. Fonseca, The role of composition, morphology and crystalline structure in the electrochemical behaviour of TiNx thin films for dry electrode sensor materials, Electrochim. Acta 55 (1) (2009) 59–67, https://doi.org/10.1016/j.electacta.2009.08.004.

[41] H. Liang, J. Xu, D. Zhou, X. Sun, S. Chu, Y. Bai, Thickness dependent microstructural and electrical properties of TiN thin films prepared by DC reactive magnetron sputtering, Ceram. Int. 42 (2) (2016) 2642–2647, https://doi.org/10.1016/j.ceramint.2015.10.070.

[42] L.A. Cyster, K.G. Parker, T.L. Parker, D.M. Grant, The effect of surface chemistry and nanotopography of titanium nitride (TiN) films on 3T3-L1 fibroblasts, J. Biomed. Mater. Res., Part A 67 (1) (2003) 138–147, https://doi.org/10.1002/jbm.a.10087.

[43] W. Spengler, R. Kaiser, A.N. Christensen, G. Müller-Vogt, Raman scattering, superconductivity, and phonon density of states of stoichiometric and nonstoichiometric TiN, Phys. Rev. B 17 (3) (Feb. 1978) 1095–1101, https://doi.org/10.1103/PhysRevB.17.1095.

[44] H.C. Barshilia, K.S. Rajam, Raman spectroscopy studies on the thermal stability of TiN, CrN, TiAlN coatings and nanolayered TiN/CrN, TiAlN/CrN multilayer coatings, J. Mater. Res. 19 (11) (2004) 3196–3205, https://doi.org/10.1557/JMR.2004.0444.

[45] S. Logothetidis, E.I. Meletis, G. Stergioudis, A.A. Adjaottor, Room temperature oxidation behavior of TiN thin films, Thin Solid Films 338 (1–2) (1999) 304–313, https://doi.org/10.1016/S0040-6090(98)00975-4.

[46] A. Fujishima, X. Zhang, D.A. Tryk, TiO2 photocatalysis and related surface phenomena, Surf. Sci. Rep. 63 (12) (2008) 515–582, https://doi.org/10.1016/j.surfrep.2008.10.001.

[47] M. Toupin, T. Brousse, D. Bélanger, Charge storage mechanism of MnO2 electrode used in aqueous electrochemical capacitor, Chem. Mater. 16 (16) (2004) 3184–3190, https://doi.org/10.1021/cm049649j.

[48] Y. Lu, H. Lyu, A.G. Richardson, T.H. Lucas, D. Kuzum, Flexible neural electrode array based-on porous graphene for cortical microstimulation and sensing, Sci. Rep. 6 (September) (2016) 1–9, https://doi.org/10.1038/srep33526.

[49] A.S. Pranti, A. Schander, A. Bödecker, W. Lang, PEDOT: PSS coating on gold microelectrodes with excellent stability and high charge injection capacity for chronic neural interfaces, Sensor. Actuator. B Chem. 275 (March) (2018) 382–393, https://doi.org/10.1016/j.snb.2018.08.007.